PHYSICAL REVIEW E, VOLUME 65, 016410

Experimental measurements of deep directional columnar heating by laser-generated relativistic electrons at near-solid density

J. A. Koch,[1] M. H. Key,[1] R. R. Freeman,[2] S. P. Hatchett,[1] R. W. Lee,[1] D. Pennington,[1] R. B. Stephens,[3] and M. Tabak[1]
[1]*University of California, Lawrence Livermore National Laboratory, P.O. Box 808, L-481, Livermore, California 94551*
[2]*Department of Applied Science, University of California, Davis, Davis, California 95616*
[3]*General Atomics, San Diego, California 92186*

(Received 30 April 2001; published 18 December 2001)

In our experiments, we irradiated solid CH targets with a 400 J, 5 ps, $3\times10^{19}\,\mathrm{W/cm^2}$ laser, and we used x-ray imaging and spectroscopic diagnostics to monitor the keV x-ray emission from thin Al or Au tracer layers buried within the targets. The experiments were designed to quantify the spatial distribution of the thermal electron temperature and density as a function of buried layer depth; these data provide insights into the behavior of relativistic electron currents which flow within the solid target and are directly and indirectly responsible for the heating. We measured ~200–350 eV temperatures and near-solid densities at depths ranging from 5 to 100 μm beneath the target surface. Time-resolved x-ray spectra from Al tracers indicate that the tracers emit thermal x rays and cool slowly compared to the time scale of the laser pulse. Most intriguingly, we consistently observe annular x-ray images in all buried tracer-layer experiments, and these data show that the temperature distribution is columnar, with enhanced heating along the edges of the column. The ring diameters are much greater than the laser focal spot diameter and do not vary significantly with the depth of the tracer layer for depths greater than 30 μm. The local temperatures are 200–350 eV for all tracer depths. We discuss recent simulations of the evolution of electron currents deep within solid targets irradiated by ultra-high-intensity lasers, and we discuss how modeling and analytical results suggest that the annular patterns we observe may be related to locally strong growth of the Weibel instability. We also suggest avenues for future research in order to further illuminate the complex physics of relativistic electron transport and energy deposition inside ultra-high-intensity laser-irradiated solid targets.

DOI: 10.1103/PhysRevE.65.016410 PACS number(s): 52.38.−r, 52.50.Jm, 52.70.La

I. INTRODUCTION

Chirped pulse amplification (CPA) techniques [1] can provide laser irradiances exceeding $I=10^{20}\,\mathrm{W/cm^2}$, and this enables experimental study of relativistic laser-plasma interactions. In this regime, electron quiver energies within the laser field exceed the electron rest energy [1,2], and self-focusing [3,4], hole boring [5], and critical-density absorption of the laser beam convert laser energy into an intense directed beam of relativistic electrons with a suprathermal temperature T_{hot} approximately proportional to $\sqrt{I\lambda^2}$, where λ is the laser wavelength [6]. These electrons can efficiently heat high-density matter. The fast-ignitor scheme [7] for inertial-confinement fusion (ICF) [8] proposes to utilize this process to ignite precompressed thermonuclear fuel with MeV electrons produced by a ~10 ps, $I\lambda^2\sim10^{19}\,\mathrm{W\,\mu m^2/cm^2}$ laser pulse; however, the physics of fast ignition, particularly the transport of energy by relativistic electrons, is still at an early stage of investigation [9]. The production of hot, dense matter is also of general interest for laboratory and astrophysical plasma physics, particularly if large, long-lived, and reasonably homogeneous volumes can be efficiently created which would allow plasma properties such as opacity to be investigated.

Energy transport by intense laser-generated relativistic electron beams is complex, since strong induced electric and magnetic fields modify the current flow. Space-charge electric fields reduce electron penetration into dense targets [10], and induce a strong charge-return current which can itself heat the target material. Fokker-Planck modeling [11,12] and some experiments [13,14] indicate that the net forward relativistic electron current becomes collimated due to its self-generated magnetic field, and this magnetic field may in turn be modified by conductivity discontinuities in a layered target [15]. Particle-in-cell (PIC) simulations show that the electron flow filaments at high densities due to a Weibel-like instability [16], and that these filaments subsequently coalesce, resulting in a dramatic nonlinear energy loss mechanism [17]. Hybrid three-dimensional (3D) PIC codes have also been recently applied to this problem [18–20]. These codes treat the relativistic electrons by PIC methods but treat the thermal electrons as a fluid within a stationary ion distribution, thereby allowing more of the relevant physics to be incorporated into tractable simulations. However, realistic simulations of real experimental conditions remain extremely challenging or impossible in many cases.

Many complex processes affect the deep heating of solid matter by laser-generated relativistic electrons and their associated return currents, and the theoretical unraveling of these processes is hampered by the difficulties inherent in simulating microscopically detailed behavior over large spatial and temporal scales. Experimental data are therefore essential, and often guide research in the field of ultra-high-intensity laser-matter interactions. Earlier experiments investigated thermal [21–23] and relativistic [24] heating within solid targets by laser-generated electrons; however, the former experiments are not directly relevant to the present problem of relativistic electron transport, and the depths accessible in the latter experiments did not exceed the depth of the laser ablation zone. Neither set of experiments utilized x-ray imaging data to show the spatial temperature

1063-651X/2001/65(1)/016410(9)/$20.00

distributions. Previous optical pyrometry measurements have given space resolved heating data from the rear surfaces of foil targets [25], and these have been complemented by measurements of optical probe absorption [26] and optical transition radiation [27]. However, rear-surface effects complicate the interpretation of these data [12]. None of these experiments, therefore, were able to investigate relativistic electron transport and energy deposition deep within solid targets.

In our experiments [28], we use x-ray spectroscopy of thin metal tracer layers buried within solid plastic targets to diagnose the local temperature and density when the surface of the target is irradiated by a petawatt-class laser [29]. We complement these data with x-ray imaging data, which diagnose the local temperature spatial distribution and allow us to extrapolate our spectroscopic temperature measurements to greater depths within the targets. Our data show nearly depth-independent local temperatures and densities for initial tracer depths up to 100 μm, a distance equivalent to $\sim$12 times the vacuum laser focus diameter and well beyond the region where laser ablation might perturb the local density. Our data also show that the heating is strongly collimated, with increased temperatures along the edges of the observed columnar structure. The data support an emerging picture of magnetically collimated relativistic electron transport and energy deposition in ultra-high-intensity laser-irradiated solid targets, but also pose additional questions for further experimental and theoretical research.

II. PETAWATT LASER EXPERIMENTS

In our experiments, a 1.054 μm wavelength, 400 J laser [29], focused to an 8 μm diameter (full width at half maximum intensity, or FWHM) spot with an $f/3$ parabolic mirror, achieved peak vacuum irradiances of $3\times10^{19}\,\mathrm{W/cm^2}$ with 5 ps pulses. Some experiments were also performed using 20 ps pulses with proportionally reduced irradiances. The laser produces a 4 ns duration, $\sim10^{-4}$ energy-contrast amplified spontaneous emission (ASE) pedestal and an $\sim3\times10^{-4}$ leakage prepulse 2 ns before the main pulse. The ASE and prepulse have little effect on the deeply buried tracer layers, as will be discussed below in Sec. IV; however, it is important to keep in mind that the main part of the laser pulse interacts with a preformed plasma, rather than with a solid/vacuum interface. In separate experiments [30], the electron density along the laser axis was measured to be $3\times10^{19}\,\mathrm{cm^{-3}}$ in a plane 70 μm from a solid CH target, and the density fell exponentially at greater distances with a scale length of 40 μm.

Each target was solid CH containing a 0.5 μm thick tracer layer of Al or Au. The laser-irradiated surface was CH in all cases, and the tracer layers were buried 5 to 200 μm below the front surface. We used two types of target for different diagnostic geometries. The first type of target was 5–50 μm CH, 0.5 μm Al or Au, and 100 μm CH; these targets were diagnosed from the front (5–50 μm CH side). The second type of target was 50–200 μm CH, 0.5 μm Au, and 5 μm CH; these targets were diagnosed from the rear (5 μm CH side) in order to minimize attenuation of the metal-tracer x-ray emission by thick CH. The front CH layer was irradiated at 0° or 45° p polarized, and each layer covered the full $1.5\times1.5\,\mathrm{mm^2}$ area of the targets. CH layers greater than 10 μm thick were polyethylene (CH_2, 0.92 g/cm^3), while thinner CH layers were evaporated paralyne-*N* (CH, 1.1–1.2 g/cm^3). For targets requiring a thick CH layer to be bonded to a thick substrate, a thin ($\sim$1 μm) diluted PVA (C_2H_4O) glue was used.

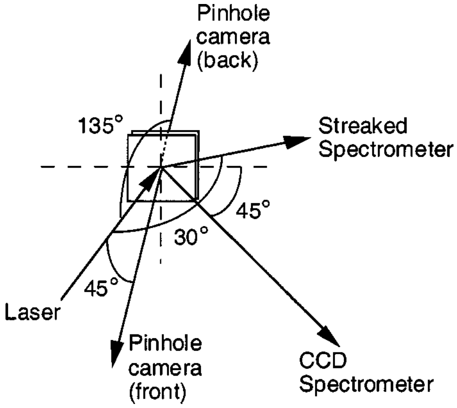

FIG. 1. Sketch of the experimental geometry for front-view and rear-view targets. The spectrometers were operated only on front-view experiments with Al tracers.

Three diagnostics viewed the x-ray emission from the Al or Au tracer layers. The first was a pinhole camera, with a 17×17 array of 10 μm pinholes in a 50 μm Ta substrate projecting $\sim18\times$ magnification images onto film or an x-ray charge-coupled device (CCD) through approximately 38 μm of Be filtering. The camera imaged the front or the back of the target, depending on the experiment, with a spatial resolution of $\sim$10 μm for x-ray energies greater than 1.5 keV. The second diagnostic was a concave-spherical mica crystal spectrometer, which delivered a spectral resolution $\Delta E/E < 2.5\times10^{-3}$ onto an x-ray CCD; the optical geometry we used [31] precluded simultaneous spatial resolution. The third diagnostic was a convex-cylindrical potassium hydrogen phthalate (KAP) crystal spectrometer, which delivered a spectral resolution $\Delta E/E < 5\times10^{-3}$ onto a streak camera with a time resolution of 25–80 ps depending on the experiment. The streak camera time resolution was much longer than the laser pulse duration, but was adequate to resolve the main features of the x-ray line emission time histories, as will be discussed below. The spectrometers were operated on front-view Al-tracer experiments only. The geometry of the experiments is shown in Fig. 1.

III. EXPERIMENTAL DATA

X-ray spectroscopy allows us to measure local electron temperatures and densities for front-view Al-tracer experiments, where the crystal spectrometers were operated. We use the spectrally integrated Al XII line ratio $(2p^2\,{}^1D_2\text{–}1s2p\,{}^1P_1)/(1s3p\text{-}1s^2)$, He-$J$/He-$\beta$, as a bulk electron temperature (T_e) diagnostic by fitting the measured ratios to simulated local thermodynamic equilibrium (LTE) optically thin spectra from the code TOTAL [32]. Because of

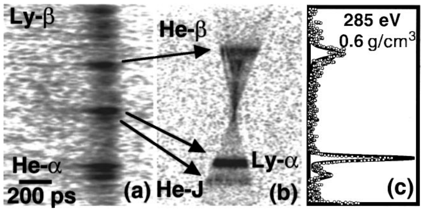

FIG. 2. KAP spectrometer (a) and mica spectrometer (b) from an Al layer 10 μm deep. Time is from right to left in (a), and the conical shape in (b) results from the focusing geometry [31]. A TOTAL fit [32] to the mica data is shown in (c) along with the inferred T_e and ρ.

the integration over the line profiles, this ratio is independent of bulk electron density N_e and instrument resolution, and based on scaling from other data [33] it is expected to be valid *despite a strong suprathermal electron flux* when $N_e > 2\times10^{22}\,\mathrm{cm}^{-3}$. This condition is satisfied in our experiments, and the high density also supports the use of LTE kinetics. The maximum optical depth for the He-J and He-β lines is predicted to be 0.6, justifying the optically thin approximation in the simulations. The He-J/He-β ratio is expected to be a more reliable measure of bulk T_e than the He-β/Ly-β ratio [33,24], since it is a direct measure of thermal electron temperature that is relatively insensitive to any high-energy suprathermal electron distribution, and isoelectronic lines are more likely to be emitted from the same spatial regions. For a density diagnostic, we fitted the blue-wing half-width of the He-β line to simulated spectra from the code FLY [34]. These simulations used steady-state kinetics and realistic opacities derived from a constant 2.7 g/cm$^3\times0.5\,\mu$m areal density (ρR) at the T_e values inferred from the TOTAL simulations. Representative data and spectra are shown in Fig. 2. All data were corrected for energy-dependent filter transmission, crystal peak reflectivity, and detector efficiency, and the simulated spectra were smoothed by the measured spectral resolution prior to comparison with the data. Analysis then allows the local bulk electron temperature and density to be measured.

Self-consistent time-integrated T_e and mass density (ρ) data are shown in Fig. 3, along with error bars representing the estimated effects of random and possible systematic errors. For Al tracers at 5–30 μm depths, we find $T_e = 270-340$ eV and $\rho = 0.25-0.95$ g/cm^3, corresponding to $N_e = (0.7-2.0)\times10^{23}\,\mathrm{cm}^{-3}$. We do not observe any significant dependence of T_e or ρ upon tracer depth, suggesting nearly isothermal heating at constant near-solid density. Al spectra from 50 μm depths were also observed, but the data were too weak for quantitative analysis. Subsolid Al densities are expected by pressure-balance arguments [$(\overline{Z}+1)\rho/A$ is approximately constant, where Z is the number of electrons/ion and A is the atomic number], and the Al layer would expand to $\sim$1.2 g/cm^3 when surrounded by isothermal solid-ρ CH using this simple estimate.

Streaked spectra show that the Al emission persists long after the laser pulse, with a duration of $\sim$70 ps FWHM as determined from the compiled time-resolved data. This supports the conclusion that the Al emission is *thermal* (rather than induced by transient relativistic electron currents), and that the Al cools gradually by conduction. This conclusion is also supported by consideration of the relevant excitation, deexcitation, and collisional stopping rates. Time-dependent kinetics modeling with FLY [34] indicates that once the suprathermal electron flux subsides the Al level populations will achieve a steady-state equilibrium within 10 ps. Suprathermal electrons will stop in the solid-density CH substrate with a characteristic time on the order of the 5 ps laser pulse duration or less [35]; refluxing electrons will be further slowed after removing ions from the target surfaces, and will also be redistributed in space. Transient ground- and excited-state population imbalances would therefore be expected to damp over time scales much shorter than the observed emission durations, and shorter than the 25–80 ps time resolution of the streak camera.

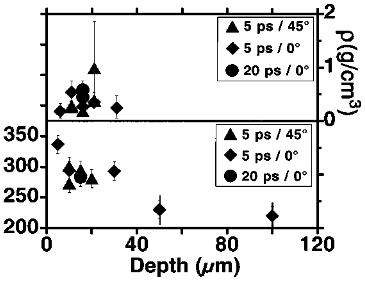

FIG. 3. Spectroscopic T_e and ρ data from the buried Al experiments (depths up to 30 μm) along with inferred T_e from the Au experiments (50 and 100 μm depths). Uncertainties are estimated from known sources of random and systematic errors, and data from both spectrometers are included. The pulse durations and the target angles of incidence are shown in the legends.

The He-β linewidth is constant in time, indicating constant density over the emission duration, but it appears 20–50 ps later than the He-J line. Time-varying He-J/He-β ratios from a single experiment with a 30 μm deep Al layer suggest that peak temperatures may be as high as $\sim$450 eV, but the other data do not show any significant time dependence to the measured electron temperatures. We note that the He-β/Ly-β ratio indicates time-integrated temperatures of 450–550 eV, although this ratio is probably less reliable, as noted above. We also observe the appearance of satellites on the red wing of the Ly-α line at greater depths (Fig. 4). These satellite features peak early in time, and are possibly emitted from hole states populated by inner-shell collisional ionization and excitation [36]; similar features dominate spectra obtained with fast-rising CPA laser irradiation of solid Al and Mg targets [37]. The appearance of these satellites is consistent with excitation and ionization of near-solid-density matter by suprathermal electrons.

We do not have spectroscopic data for tracer depths greater than 30 μm, since Al x-ray emission was weak at such depths and Au quasicontinuum x-ray emission cannot be used directly to diagnose temperature and density. However, consideration of the temperature dependence of the pinhole image brightness allows us to infer greater than 200 eV peak temperatures at depths as great as 100 μm, as will be discussed below.

Representative x-ray images from the pinhole camera are

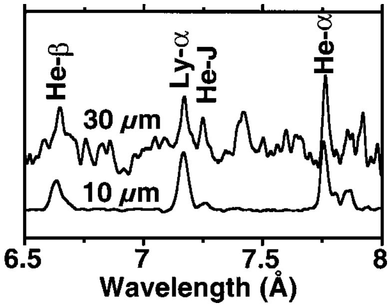

FIG. 4. Comparison of Al spectra from 10 and 30 μm depths. The temperatures inferred from the He-J/He-β ratios are nearly the same, but the deeper spectrum contains numerous satellite features which may be caused by suprathermal electrons.

shown in Fig. 5. In every buried-layer experiment where x-ray imaging data was obtained, we observed an annular pattern of emission exhibiting azimuthal structure. The diameter of the annulus varied from 50 to 120 μm depending on tracer depth (10 to 100 μm) and material (Al or Au), although our data set is insufficient to allow correlations to be discerned that might indicate a cause for these variations; the largest diameters we observed were from shallowly buried Al tracers. The annulus diameters we observe are much larger than the ~8 μm laser focal spot diameter in vacuum, and in some cases are much larger than the initial tracer depth; however, as noted above, the laser ASE and prepulse create significant preformed plasma in front of the target surface by the time of peak laser intensity, making this comparison less relevant. We return to this issue in Sec. V. In each image of Fig. 5, approximately 20 individual images from the pinhole array were averaged to improve the signal-to-noise ratio. For this averaging, we located consistent features in the images and used their coordinates together with the known constant pinhole spacing to determine the magnification and image registration; this process is expected to degrade the object resolution of the averaged images to no worse than 20 μm.

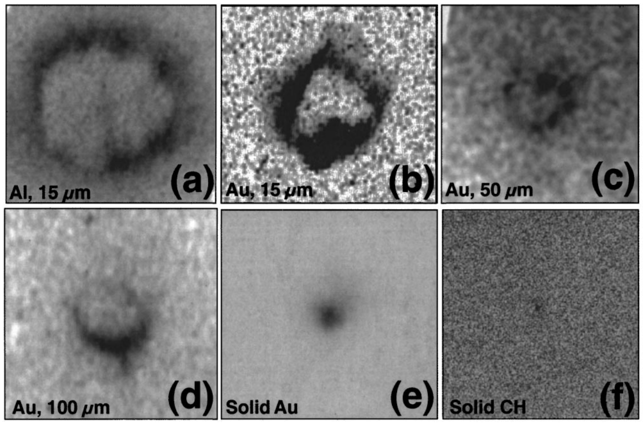

FIG. 5. X-ray pinhole images of an Al tracer 15 μm deep (a), a Au tracer 15 μm deep (b), a Au tracer 50 μm deep (c), a Au tracer 100 μm deep (d), a solid Au surface (e), and a solid CH surface (f). The image in (b) is partly saturated due to overexposure of the electronic detector. In each case, ~20 individual pinhole images from the same experiment were averaged to improve the signal-to-noise ratio, and the results were corrected for a viewing angle along the target surface normal. Each image shows a 180 μm square region of the target.

Front-view Al tracers 10–25 μm deep showed annular images with 70–120 μm inner diameters [Fig. 5(a)], typically containing several bright spots along the circumference and exhibiting a peak-to-center contrast ratio greater than 5; a front-view Au tracer 15 μm deep showed a similar (but much brighter) 70 μm diameter ring [Fig. 5(b)]. Front-view Al tracers 30–50 μm deep showed ~50 μm regions of weakly visible arclike structure, which we attribute to low signal levels that permitted only the brightest portions of the rings to be observed. Rear-view Au tracers 50–100 μm deep showed clear rings 50 μm in diameter [Figs. 5(c) and 5(d)]. We also obtained a rear-view image from a Au tracer 200 μm deep, but the exposure was too weak to exhibit structure.

In order to verify that the ring emission patterns were in fact characteristic of the tracer layers, we performed additional experiments with solid targets. Front-view solid Au and Al targets typically showed bright sub-20-μm spots [Fig. 5(e)], in dramatic contrast to the buried-layer data; more importantly, pure CH targets produced (at most) very weak spotlike images similar to the solid Al and Au data [Fig. 5(f)]. These solid-target data show that the annular patterns are emitted from the buried tracer layers, and cannot be caused by surface interactions similar to those observed in earlier experiments with laser-irradiated solids [38]. Finally, we note that the ring patterns appear to be symmetric about the target surface normal. Most experiments were performed with the laser at normal incidence, but a single experiment with the target rotated 45° (p polarized) produced an elliptical image with an orientation and aspect ratio consistent with symmetry about the target normal vector.

The Be filtering on the pinhole camera essentially eliminates x-ray energies below 1.5 keV, but does not provide any spectral discrimination of x-ray energies above 1.5 keV. However, the Al-tracer spectra show that the dominant emission below 2.5 keV is from Al lines. The spectrally and temporally integrated exposures of the x-ray spectra and the x-ray pinhole images are strongly correlated, indicating that the Al spectra are emitted from the locations that appear brightest in the images (see Fig. 6). We therefore conclude that our spectrometers measure local temperatures and densities at the spatial locations in the tracer layers that appear brightest in the x-ray images, i.e., along the circumference of the annular patterns. Conversely, the time-resolved x-ray spectra indicate that the x-ray imaging data must be prompt, since all keV x-ray emissions are observed to occur within a 70 ps time window following the laser pulse, and since there is no reason to expect significant late-time x-ray emission outside the temporal range of our streak camera, which was as long as 6 ns in some experiments.

The exposures of the Al-tracer pinhole images will scale exponentially with T_e below ~400 eV, where the emission is dominated by the optically thick He-α line in the Wien region of the thermal spectrum. Observable images were obtained with identical filtering on all the Al experiments over a dynamic range of approximately 5, and the strong scaling of Al-tracer image brightness with T_e (see Fig. 7) supports

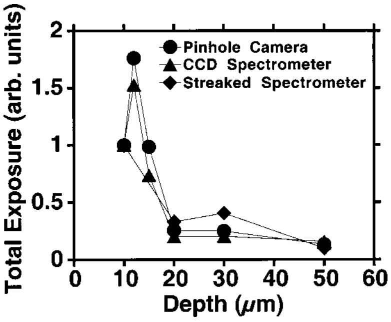

FIG. 6. Relative exposures of Al-tracer data from the pinhole camera, the CCD spectrometer, and the streaked spectrometer for various tracer depths. All data were temporally and spectrally integrated, and corrected for energy-dependent filter transmission variations. The strong correlation supports the conclusion that the bright, optically thick Al resonance lines evident in the spectra are also primarily responsible for the pinhole camera image exposures.

the conclusion of nearly depth-independent heating for depths up to 50 μm. X-ray emission from a 0.5 μm thick Au layer will be optically thick at these temperatures and densities, and therefore the Au-tracer image intensity is expected to be even more temperature sensitive than the Al-tracer image intensity; by scaling temperature with spectrally integrated blackbody image brightness (Fig. 7) and normalizing the Au image brightness at a 15 μm depth to the temperature derived from Al tracers at the same depth, we can estimate the local temperature of the Au tracer layers for depths as great as 100 μm. This scaling results in temperature estimates of approximately 220 eV for 50 μm and 100 μm depths (Fig. 3). We note that it is energetically feasible to fully ionize a 50 μm diameter, 100 μm deep column of 1 g/cm^3 CH and heat it to 300 eV, since this would require only ~8 J, or less than 3% of the available laser energy.

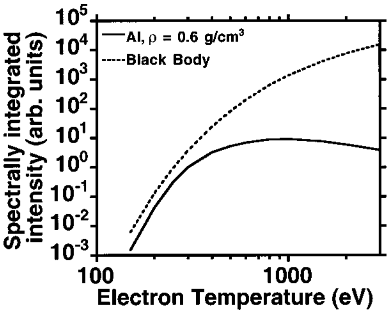

FIG. 7. Relative emission intensity as a function of electron temperature for a layer of Al at $\rho = 0.6\,\mathrm{g/cm^3}$ and $\rho R = 2.7$ g/cm$^3 \times 0.5\,\mu$m (solid line) and for a blackbody radiator (dotted line), normalized to unity for Al at 300 eV. The emission intensities were spectrally integrated over a 1.5–4.0 keV range of x-ray energies, and the spectra were corrected for energy-dependent filter transmission through 38 μm of Be. Simulated Al x-ray spectra were generated with the code FLY [34], and the simulations included detailed line shapes for all important transitions between 1.5 and 4 keV. The Al-tracer emission intensity, spectrally integrated from 1.5 to 4 keV, will scale with temperature essentially as a blackbody for $T_e < 400$ eV.

IV. DATA INTERPRETATION AND SUMMARY

The spectroscopic data directly diagnose the plasma conditions in the hot, near-solid-density regions of the tracer layers, while the x-ray imaging data show that the temperature distribution in the tracers is annular. The 5:1 dynamic range of the image brightness and the strong scaling of x-ray image brightness with temperature for both Al and Au (Fig. 7) imply that the annular emission pattern could result from the edges of the column structure being as little as 25% warmer than the material in the center of the column.

We have considered and ruled out decompression as a possible cause for the reduced x-ray emissivity at the centers of the rings. Hydrodynamic simulations of the interaction of the ~150 mJ ASE and prepulse with the buried-Al targets predict the on-axis local Al electron density at $t = 0$ as a function of initial layer depth [39]. This density is $1.5 \times 10^{22}\,\mathrm{cm}^{-3}$ for an initial depth of 15 μm, potentially resulting in a factor of ~5 reduction in per atom Al emissivity at constant $T_e = 300\,\mathrm{eV}$ [34]; however, layers at initial depths greater than 50 μm are totally unaffected by the ASE and prepulse, and the data from these deeply-buried-layer experiments do not qualitatively differ from the more shallowly buried tracer-layer data. During the 5 ps main laser pulse, we estimate a peak ponderomotive pressure $I/c \approx 17\,\mathrm{Gbar}$ and a front speed $\sqrt{P/\rho} \approx 1.3 \times 10^8$ cm/s, resulting in a hole-boring depth of ~6 μm; this agrees with other estimates [6], and is too small to reach the buried tracer layers. Later ablation of the target would proceed at ion sound speeds of $\sim 2 \times 10^7$ cm/s, too slow to reach the deeply buried tracers in ~70 ps.

Similarly, we have considered and ruled out overionization of the central portions of the tracer layers as a possible cause for the reduced x-ray emissivity at the centers of the rings. Overionization of the central portions of the Al tracer layers would require multi-keV temperatures (see Fig. 7) which were not seen in similar solid-target experiments measuring thermal D_2 neutrons [40], and overionization of the (much higher areal density and atomic number) Au tracer layers is implausible. Furthermore, we see no evidence for subsequent cooling and recombination emission, and the lack of observed central hot spots in the time-integrated images of the deeply buried tracers is inconsistent with this mechanism. Finally, the sharp intensity gradient on the inner edge of the rings is difficult to explain as a consequence of either decompression or overionization.

To summarize our experimental data, we conclude that in each of our buried tracer-layer experiments we observe an annular pattern of heating. The temperature distribution has a local minimum at the center of the ring, and the edge-to-center temperature difference may be as little as 25%. Solid-target data from Al, Au, and CH show dramatically different x-ray images, with sub-20-μm spots and, in the case of CH, weak or nonexistent exposure levels. This supports the conclusion that the ring patterns are emitted from the tracer layers themselves, as does the observed correlation between image exposure and spectra exposure on those experiments that showed clear spectral signatures of heated Al tracer material. The diameters of the rings are 50–120 μm for tracer depths of 10–100 μm, with larger diameters observed at shallower depths, and the rings appear symmetric about the target surface normal.

X-ray spectra from Al tracers buried 5–30 μm deep show a time- and space-integrated temperature of 340 eV for 5 μm depth and an essentially depth-independent temperature of $\sim$300 eV for 10–30 μm depths. The spectra also show tracer electron densities of $(0.7-2.0)\times 10^{23}\,\mathrm{cm}^{-3}$. Spectra from a 30 μm deep Al tracer suggest somewhat higher peak (in time) temperatures of 450 eV, but the other data show no significant time dependence to the temperature or density. The emission duration is $\sim$70 ps, much longer than the laser pulse duration and the relevant excitation, deexcitation, and collisional stopping time scales; this supports the conclusion of thermal x-ray emission from the tamped, high-density tracer layers, followed by gradual conductive cooling. Finally, analysis of the temperature dependence of the spectrally integrated 1.5–4.0 keV emission from Al and Au tracers allows us to infer temperatures from relative pinhole camera image exposure levels, normalized to the spectrometer data; this results in a temperature estimate of $\sim$220 eV for Au tracers at 50 and 100 μm depths.

V. THEORETICAL PREDICTIONS

Our experimental data suggest collimated energy transport by relativistic electrons within solid CH targets, with essentially depth-independent energy deposition and a slight annular peak in the heating of buried Al and Au tracer layers to $\sim$200–300 eV temperatures at near-solid density. Theoretical predictions [11,12] and experimental evidence [13,14] exist for magnetically collimated relativistic electron flow (and thus nearly depth-independent local temperature distributions), but the annular emission patterns shown in Fig. 5 were initially unexpected. Prior theoretical modeling, however, provides insights into this behavior, and we begin our discussion by reviewing these modeling results.

The importance of plasma resistivity was shown by planar one-dimensional analytic modeling of relativistic electrons penetrating a cool plasma [10]; this work also provided estimates of the electric potential. Later hybrid modeling, with a Monte Carlo/Fokker-Planck description of the relativistic electrons and a fluid description of the cold (thermal background) electrons in 2D cylindrical symmetry [11,12] revealed the important process of self-induced magnetic collimation. This collimation is caused by the relativistic electron current exceeding the cold electron return current, resulting in a net forward-directed current approximately limited to the Alfvén current ($\sim$17 γ kA, where γ is the relativistic Lorentz factor [41]). In our experiments we expect 20% conversion of the 400 J, 5 ps laser pulse into relativistic electrons with mean energy 0.7 MeV [9,42,43]. The relativistic electron density is then $\sim 5\times 10^{20}\,\mathrm{cm}^{-3}$, in a background plasma with $T_e \approx 300$ eV and $N_e \approx 10^{23}\,\mathrm{cm}^{-3}$. The resulting relativistic electron current is 29 MA, which is 770 times the Alfvén limit; this shows that almost complete return-current compensation is required for the relativistic electron beam to penetrate into the target.

A Weibel-like instability [44], with transverse magnetic and current density perturbations, has been shown to cause filamentation of the opposed hot electron currents and cold electron return currents on a time scale equal to the plasma frequency ω_p and on a spatial scale equal to the plasma skin depth c/ω_p. Two-dimensional PIC models with one axial and one transverse dimension [16,45] simulated the development of these filamentary patterns. In the following discussion, we will use the name Weibel when referring to this Weibel-like instability.

Subsequent to our experiments [28], more detailed studies of the structure of these filaments were made with 2D PIC modeling of the beam pattern in a plane perpendicular to the relativistic current axis [17,41]. This work showed the nonlinear development of the Weibel instability, with coalescence of the filaments and related collisionless heating of the background plasma. However, pure PIC models are severely limited by available computing power, and can only describe small elements of volume and time with densities much less than solid, typically $\sim 10^{22}\,\mathrm{cm}^{-3}$. These models also use periodic boundary conditions, and do not describe a beam of specified transverse shape and net current.

The first indication of a tendency for the relativistic electron flow to develop an annular pattern was seen in 3D hybrid PIC modeling [18,19]. In this model, a 10 μm diameter collimated beam of 1 MeV monoenergetic electrons carried 3 MA into solid-density Al for 300 fs. A 25 μm diameter current annulus with azimuthal peaks developed at depths exceeding 5 μm. These results were later extended to the case of an electron beam propagating through $\sim$2 eV solid-density CH [47]. In this last simulation, relativistic electron energies were related to the local laser intensity (rather than being monoenergetic), and the electron beam had a cone angle of 30° (rather than being collimated); the results showed an annular pattern developing in the relativistic electron flow, and also showed a weak annular pattern in the heating of the background plasma.

Taguchi *et al.* [20] recently developed a 3D hybrid PIC code with a Darwin approximation to describe essentially the full range of magneto hydrodynamic phenomena, and used this code to analyze the propagation of a 1 MeV electron beam, at 0.1 of the background plasma density, into plasma with an electron density of $10^{22}\,\mathrm{cm}^{-3}$. The beam diameter was circular with a 1.8 μm diameter super-Gaussian profile. This model also showed that the current density increases to form an annular peak at the edge of the beam, and that the annulus later breaks up azimuthally into multiple filaments in a manner qualitatively very similar to our experimental observations (see Fig. 5). This model specifically treated the case where the linear growth exponent of the Weibel instability is $\sim$10 at spatial wavelengths corresponding to the strong spatial Fourier components of both the edge of the beam and the growing annular peak. However, the space (1.8 μm), time (14 fs), and density (10^{22} cm^{-3}) scales were much smaller than in our experiments.

Due to the limits of available computing power, none of these models are capable of describing our specific experimental conditions. We therefore use a simpler theoretical approach [48] to analyze a process similar to that described by Taguchi *et al.* for the particular space, time, and density

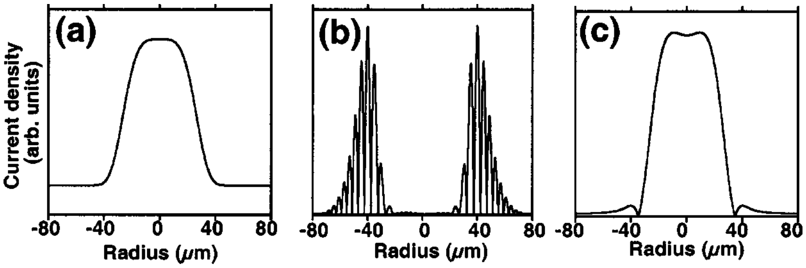

FIG. 8. Cross sections of a 60 μm diameter, fourth-power super-Gaussian input relativistic electron current spatial profile (a), the calculated current profile after 5 ps of Weibel instability growth with a growth exponent of 10 at a wavelength of 20 μm (b), and the calculated current profile with all growth exponents reduced by a factor of 10 (c). In each figure, the horizontal axis is the beam radius in micrometers, and the vertical axis is the (arbitrarily scaled) current density.

scales of our experiment. We treat this process as the growth of the Fourier components of the relativistic electron current spatial pattern at a linear Weibel growth rate. Linear perturbation analysis is used to calculate the wave-number dependence of the Weibel growth rate, and we follow earlier work [46] to solve a dispersion equation including the hot (relativistic) and cold (background) electron temperatures and the resistive collision rates. As parameters we assume a cold electron density $N_e = 3\times10^{23}\,\mathrm{cm}^{-3}$ (consistent with highly ionized 1 $\mathrm{g\,cm}^{-3}$ CH), a cold electron temperature $T_e = 300\,\mathrm{eV}$, a hot electron density $N_{\mathrm{hot}} = 5\times10^{20}\,\mathrm{cm}^{-3}$, a hot electron average energy of 1 MeV, and a hot electron transverse temperature of 0.3 MeV. For the specified background plasma, the collision frequency (normalized to the plasma frequency) is approximately 1.0 [49], while the normalized hot beam collision frequency is estimated to be 5×10^{-5} [50].

For these conditions, the Weibel growth time constant for a 20 μm wavelength perturbation, typical of the width of the annular rings we observe, is 500 fs. This would allow ~10 *e*-foldings of growth during the 5 ps laser pulse, similar to the situation analyzed by Taguchi *et al.* [20]. We Fourier analyzed (in one dimension) the transverse spatial pattern of a 60 μm diameter, fourth-power super-Gaussian electron beam [Fig. 8(a)], and then imposed exponential growth of the Fourier spectrum using growth exponents from the linear growth rate analysis. This procedure generated a pronounced 80 μm diameter annular pattern [Fig. 8(b)]; scaling down all growth exponents by a factor of 10 eliminated the effect [Fig. 8(c)]. Application of a similar analysis to the case treated by Taguchi *et al.* showed a similar enhancement of the current density at the edge of the beam to that calculated in their more detailed modeling.

These results suggest that the evolution of an annular pattern, as we observed in our experiments, may be characteristic of Weibel growth during our 5 ps laser pulses, and that it might not be a pronounced feature in other experiments with subpicosecond pulse durations. We emphasize again that our experiments show an annular pattern in *heating*, and do not directly measure the spatial pattern of the *forward electron current*. However, given the theoretical results of Gremillet *et al.* [18] discussed above, and given that only a small (~25%) temperature variation across the annulus is sufficient to explain our observed emissivity variations, we believe that the Weibel-instability-driven development of an annular pattern in the forward current provides the most likely explanation of our experimental data.

A much more speculative possibility arises from consideration of the fact that the Alfvén current limit for an annular current pattern increases linearly with increasing diameter-to-thickness ratio of the annulus. This suggests the possibility that in the nonlinear limit, where Weibel filaments have coalesced until each carriers one Alfvén current, there may be a favored (more rapid) evolution of further coalescence events into an annular current pattern. This would avoid the otherwise necessary dissipation of 50% of the current, which is seen in PIC modeling of coalescence events when two filaments each carry one Alfvén current [41]. Development of an explicit physical model of this process would be necessary for it to be treated as more than an intriguing speculation.

We note again that the diameters of the annular patterns we observe in our experiments are much larger than the nominal laser focal spot diameter, and we do not resolve the reasons for this observation here. We know that the vacuum laser focal spot had broad wings, with 70% of the energy outside the Airy disk [29], and we also know that relativistic self-focusing of laser light in preformed plasma strongly modifies the pattern of laser intensity on the target [3,40]. We speculate that the initial electron beam pattern, which may bear little resemblance to the vacuum light intensity pattern at focus, may have had a relatively sharp discontinuity at the location of the observed annular peak, and that strong harmonic components were amplified by the Weibel instability to form the annulus. We further speculate that blocking of the energy transport and trapping of energy at the surface of the target by the nonlinear Weibel instability [41] may force an increase in the area over which energy enters the target. We cannot, however, draw any definite conclusion on these issues without further experimental studies and theoretical work.

We do not address the question of the relative importance of return-current heating in our experiments. This is not a critical point in our interpretation of the annular patterns, however, since the return current will be strongest where the relativistic forward current is strongest. This must be the case in our experiments, where the forward current of hot electrons is estimated to be 770 times the Alfvén current, and local neutralization of the hot current by the cold return current is therefore required.

To summarize our discussion of theoretical models, we believe that our observed annular heating pattern and its azimuthal structure may be linked to strong Weibel instability growth at locations where the forward-directed current has strong transverse gradients. The net collimation of the energy transport can be linked to the azimuthal magnetic field generated by a net forward electron current of close to one Alfvén current.

Collimated energy transport is highly beneficial for fast-ignition ICF [7]. However, an annular current pattern, with a diameter large compared with the nominal laser focal spot diameter, would raise the threshold energy for fast ignition approximately proportionally to the square of the diameter ratio. A recent estimate, using an annular electron beam of inner radius 20 μm and outer radius 50 μm, based on the energy transport parameters of our experiments [42] and assuming a compressed fuel density of 460 $\mathrm{g\,cm^{-3}}$, put the ignition threshold at 100 kJ in the electron beam [51]. This compares to the ideal case of 8.3 kJ for a 26 μm diameter spot, and is roughly consistent with the expected quadratic scaling with beam diameter.

A complete understanding of the heating distributions we observe must await significant progress in developing more advanced simulations, which at this time cannot satisfactorily model our experimental conditions. Several other issues may also need to be addressed in order to obtain a satisfactory theoretical understanding of our data. First, existing 3D hybrid simulations do not treat laser propagation within preformed underdense plasma, and instead specify as inputs the spatial and energy distributions of relativistic electrons at the front surface of the target. However, relativistic laser propagation through underdense plasma has been investigated separately and shown to strongly affect laser intensity profiles at critical density [3]; in general, the electron source spatial distribution may bear little resemblance to the vacuum laser intensity distribution at focus. A consistent treatment of laser-generated electron transport through solid targets, including laser-plasma interactions in plasma created by realistic levels of laser ASE and prepulse, would be valuable; 3D PIC modeling has linked the laser-plasma interaction to the electron source, but not yet for a realistic laser beam or preformed plasma scale length. Second, conductivity discontinuities (i.e., metal tracers) could affect energy deposition in the vicinity of the tracers, as has been noted earlier [15]. In this sense, metal tracer layers may be perturbative; the effects of these conductivity discontinuities are not treated in existing simulations. Finally, the repeatability of our observations, and their striking nature, suggest that additional experiments would be valuable. We suggest that prepulse and intensity parameter scans and space-resolved spectroscopy could be valuable, and, in particular, it would be valuable to directly characterize the spatial distribution of forward electron current within the target. This could be accomplished with x-ray imaging at much higher photon energies, possibly observing monochromatic $K\alpha$ x rays from higher-Z tracer layers [52].

VI. CONCLUSIONS

In conclusion, we have observed highly directional heating of near-solid-density material induced by relativistic electrons generated by an intense short pulse laser. The heating is relatively uniform and deep within the solid target, and it shows a clear, reproducible columnar structure with enhanced heating at the edges of the column. We believe this annular heating pattern may be related to strong Weibel instability growth where the input electron beam current has sharp transverse gradients. Our measurements are important for achieving an understanding of laser-generated relativistic electron transport in solid matter, especially in light of the significant recent activity in modeling this process. A clear understanding of all the physical mechanisms involved in relativistic electron transport through solid materials, and their successful inclusion in refined models, is essential for the development of the fast-ignitor fusion concept, and achieving this understanding will require further improvements in simulation capabilities as well as additional critical experimental data.

ACKNOWLEDGMENTS

We owe special thanks to Y. Sentoku, L. Gremillet, and T. Taguchi for valuable discussions and communication of their unpublished modeling results. We also gratefully acknowledge S. Alvarez, J. Bower, C. Brown, E. M. Campbell, R. Costa, A. Faenov, B. Hammel, J. Kilkenny, R. Kodama, O. Landen, A. MacKinnon, K. Mima, M. Moran, A. Offenberger, M. Perry, T. Pikuz, R. Robinson, C. Sangster, R. Snavely, K. Tanaka, M. Tsukamoto, R. Wallace, S. Wilks, and K. Yasuike for their contributions and support. This work was performed under the auspices of the U.S. Department of Energy by the University of California Lawrence Livermore National Laboratory under Contract No. W-7405-ENG-48, with the additional support of General Atomics and the University of California, Davis.

---

[1] M. D. Perry and G. Mourou, Science **264**, 917 (1994).
[2] P. Gibbon and E. Förster, Plasma Phys. Controlled Fusion **38**, 769 (1996).
[3] A. Pukhov and J. Meyer-ter-Vehn, Phys. Rev. Lett. **76**, 3975 (1996).
[4] M. Borghesi, A. J. MacKinnon, L. Barringer, R. Gaillard, L. A. Gizzi, C. Meyer, O. Willi, A. Pukhov, and J. Meyer-ter-Vehn, Phys. Rev. Lett. **78**, 879 (1997).
[5] R. Kodama, K. Takahashi, K. A. Tanaka, M. Tsukamoto, H. Hashimoto, Y. Kato, and K. Mima, Phys. Rev. Lett. **77**, 4906 (1996).
[6] S. C. Wilks, Phys. Fluids B **5**, 2603 (1993).
[7] M. Tabak, J. Hammer, M. E. Glinsky, W. L. Kruer, S. C. Wilks, J. Woodworth, E. M. Campbell, M. D. Perry, and R. J. Mason, Phys. Plasmas **1**, 1626 (1994).
[8] J. D. Lindl, Phys. Plasmas **2**, 3933 (1995).
[9] M. H. Key, K. Estabrook, B. Hammel, S. Hatchett, D. Hinkel, J. Kilkenny, J. Koch, W. Kruer, B. Langdon, B. Lasinski, R.

Lee, B. MacGowan, J. Moody, M. Moran, A. Offenberger, D. Pennington, M. Perry, T. Phillips, C. Sangster, M. Tabak, G. Tietbohl, M. Tsukamoto, K. Wharton, and S. Wilks, Phys. Plasmas **5**, 1966 (1998), and references therein.
[10] A. R. Bell, J. R. Davies, S. Guérin, and H. Ruhl, Plasma Phys. Controlled Fusion **39**, 653 (1997).
[11] J. R. Davies, A. R. Bell, M. G. Haines, and S. M. Guérin, Phys. Rev. E **56**, 7193 (1997).
[12] J. R. Davies, A. R. Bell, and M. Tatarakis, Phys. Rev. E **59**, 6032 (1999).
[13] M. Tatarakis, J. R. Davies, P. Lee, P. A. Norreys, N. G. Kassapakis, F. N. Beg, A. R. Bell, M. G. Haines, and A. E. Dangor, Phys. Rev. Lett. **81**, 999 (1998).
[14] L. Gremillet, F. Amiranoff, S. D. Baton, J.-C. Gauthier, M. Koenig, E. Martinolli, F. Pisani, G. Bonnaud, C. Lebourg, C. Rousseaux, C. Toupin, A. Antonicci, D. Batani, A. Bernardinello, T. Hall, D. Scott, P. Norreys, H. Bandulet, and H. Pépin, Phys. Rev. Lett. **83**, 5015 (1999).
[15] A. R. Bell, J. R. Davies, and S. M. Guérin, Phys. Rev. E **58**, 2471 (1998).
[16] B. F. Lasinski, A. B. Langdon, S. P. Hatchett, M. H. Key, and M. Tabak, Phys. Plasmas **6**, 2041 (1999).
[17] M. Honda, J. Meyer-ter-Vehn, and A. Pukhov, Phys. Plasmas **7**, 1302 (2000).
[18] L. Gremillet *et al.*, in *Inertial Fusion Sciences and Applications 99*, edited by C. Labaune, W. Hogan, and K. Tanaka (Elsevier, Paris, 2000), p. 451; (private communication).
[19] C. Toupin, Ph.D. thesis, Université de Paris–Sud, UFR Scientifique d'Orsay, No. d'ordre 5987, 1999.
[20] T. Taguchi, T. M. Antosen, Jr., C. S. Liu, and K. Mima (unpublished).
[21] G. J. Tallents, M. H. Key, P. Norreys, D. Brown, J. Dunn, and H. Baldis, Phys. Rev. A **40**, 2857 (1989).
[22] G. Guethlein, M. E. Foord, and D. Price, Phys. Rev. Lett. **77**, 1055 (1996).
[23] A. Saemann, K. Eidmann, I. E. Golovkin, R. C. Mancini, E. Andersson, E. Förster, and K. Witte, Phys. Rev. Lett. **82**, 4843 (1999).
[24] J. A. Koch, C. A. Back, C. Brown, K. Estabrook, B. A. Hammel, S. P. Hatchett, M. H. Key, J. D. Kilkenny, O. L. Landen, R. W. Lee, J. D. Moody, A. A. Offenberger, D. Pennington, M. D. Perry, M. Tabak, V. Yanovsky, R. J. Wallace, K. B. Wharton, and S. C. Wilks, Laser Part. Beams **16**, 225 (1998).
[25] R. Kodama (unpublished).
[26] E. Martinolli (unpublished).
[27] J. Santos (unpublished).
[28] J. A. Koch, S. P. Hatchett, M. H. Key, R. W. Lee, D. Pennington, R. B. Stephens, and M. Tabak, *Inertial Fusion Sciences and Applications 99* (Ref. [18]), p. 463.
[29] M. D. Perry, D. Pennington, B. C. Stuart, G. Tietbohl, J. A. Britten, C. Brown, S. Herman, B. Golick, M. Kartz, J. Miller, H. T. Powell, M. Vergino, and V. Yanovsky, Opt. Lett. **24**, 160 (1999).
[30] A. J. MacKinnon *et al.*, Bull. Am. Phys. Soc. **44** (7), 319 (1999).
[31] J. A. Koch, O. L. Landen, T. Barbee, Jr., G. Bennett, C. Brown, P. Celliers, G. Collins, L. Da Silva, S. Glendinning, S. Haan, B. Hammel, W. Hsing, D. Kalantar, M. Key, J. Seely, L. Suter, and F. Weber, Rev. Sci. Instrum. **70**, 525 (1999).
[32] B. Talin, A. Calisti, S. Ferri, M. Koubiti, T. Meftah, C. Mosse, L. Mouret, R. Stamm, S. Alexiou, R. W. Lee, and L. Klein, J. Quant. Spectrosc. Radiat. Transf. **58**, 953 (1997), and references therein.
[33] F. B. Rosmej, J. Phys. B **28**, L747 (1995).
[34] R. W. Lee and J. T. Larsen, J. Quant. Spectrosc. Radiat. Transf. **56**, 535 (1996).
[35] This topic is complex since nonclassical effects increase the effective stopping power; see, for example, T. A. Hall, S. Ellwi, D. Batani, A. Bernardinello, V. Masella, M. Koenig, A. Benuzzi, J. Krishnan, F. Pisani, A. Djaoui, P. Norreys, D. Neely, S. Rose, M. H. Key, and P. Fews, Phys. Rev. Lett. **81**, 1003 (1998); C. Deutsch, H. Furukawa, K. Mima, M. Murakami, and K. Nishihara, *ibid.* **77**, 2483 (1996); and Refs. [7], [10], and [41].
[36] F. B. Rosmej, B. A. Bryunetkin, A. Ya. Faenov, I. Yu. Skobelev, M. P. Kalashnikov, P. V. Nickles, and M. Schnürer, J. Phys. B **29**, L299 (1996).
[37] F. B. Rosmej, A. Ya. Faenov, T. A. Pikuz, I. Yu. Skobelev, A. E. Stepanov, A. N. Starostin, V. S. Rerikh, V. A. Makhrov, F. Flora, S. Bollanti, P. Di Lazzaro, T. Letardi, K. Vigli-Papadaki, A. Nottola, A. Grilli, L. Palladino, A. Reale, A. Scafati, and L. Reale, JETP Lett. **65**, 708 (1997).
[38] M. D. J. Burgess, B. Luther-Davies, and K. A. Nugent, Phys. Fluids **28**, 2286 (1985).
[39] LASNEX; see G. B. Zimmerman and W. L. Kruer, Comments Plasma Phys. Controlled Fusion **2**, 51 (1975).
[40] M. H. Key, E. M. Campbell, T. E. Cowan, S. P. Hatchett, E. A. Henry, J. A. Koch, A. B. Langdon, B. F. Lasinski, A. MacKinnon, A. A. Offenberger, D. M. Pennington, M. D. Perry, T. J. Phillips, T. C. Sangster, M. S. Singh, R. A. Snavely, M. A. Stoyer, M. Tsukamoto, K. B. Wharton, and S. C. Wilks, J. Fusion Energy **17**, 231 (1998).
[41] M. Honda, J. Meyer-ter-Vehn, and A. Pukhov, Phys. Rev. Lett. **85**, 2128 (2000).
[42] S. P. Hatchett, C. G. Brown, T. E. Cowan, E. A. Henry, J. Johnson, M. H. Key, J. A. Koch, A. B. Langdon, B. F. Lasinski, R. W. Lee, A. J. MacKinnon, D. M. Pennington, M. D. Perry, T. W. Phillips, M. Roth, T. C. Sangster, M. S. Singh, R. A. Snavely, M. A. Stoyer, S. C. Wilks, and K. Yasuike, Phys. Plasmas **7**, 2076 (2000).
[43] K. B. Wharton, S. P. Hatchett, S. C. Wilks, M. H. Key, J. D. Moody, V. Yanovsky, A. A. Offenberger, B. A. Hammel, M. D. Perry, and C. Joshi, Phys. Rev. Lett. **81**, 822 (1998).
[44] E. W. Weibel, Phys. Rev. Lett. **2**, 83 (1959).
[45] J. C. Adam and A. Heron (private communication); Technical Report No. RAL-TR-1988-085, Rutherford Appleton Laboratory, U.K., 1999 (unpublished).
[46] Y. Sentoku, K. Mima, S. Kojima, and H. Ruhl, Phys. Plasmas **7**, 689 (2000).
[47] L. Gremillet (private communication).
[48] M. H. Key *et al.* (unpublished).
[49] Y. T. Lee and R. M. More, Phys. Fluids **27**, 1273 (1984).
[50] J. D. Jackson, *Classical Electrodynamics*, 2nd. ed. (Wiley, New York, 1975).
[51] S. Atzeni, Phys. Plasmas **6**, 3316 (1999).
[52] J. A. Koch, O. L. Landen, T. W. Barbee, Jr., P. Celliers, L. B. Da Silva, S. G. Glendinning, B. A. Hammel, D. H. Kalantar, C. Brown, J. Seely, G. R. Bennett, and W. Hsing, Appl. Opt. **37**, 1784 (1998).